Event-based versus particle image velocimetry for cardiac flow analysis in a left-heart simulator

RESEARCH ARTICLE | FEBRUARY 18 2026

Event-based versus particle image velocimetry for cardiac flow analysis in a left-heart simulator

E. Amico ; M. Zannone ; E. Torta ; G. Mastronuzzi ; D. Pecchio; D. Gallo ; J. Serpieri ; G. Cafiero ; U. Morbiducci

Physics of Fluids 38, 021916 (2026)
https://doi.org/10.1063/5.0315234

Event-based versus particle image velocimetry for cardiac flow analysis in a left-heart simulator

Cite as: Phys. Fluids **38**, 021916 (2026); doi: 10.1063/5.0315234
Submitted: 4 December 2025 · Accepted: 27 January 2026 ·
Published Online: 18 February 2026

E. Amico,[1] M. Zannone,[1] E. Torta,[1] G. Mastronuzzi,[1] D. Pecchio,[2] D. Gallo,[1] J. Serpieri,[1] G. Cafiero,[1] and U. Morbiducci[1,a)]

AFFILIATIONS

[1]Department of Mechanical and Aerospace Engineering, Politecnico di Torino, Corso Duca Degli Abruzzi 24, 10129 Turin, Italy
[2]Affluent Medical SA, 320 Avenue Archimède, Les Pléiades III Batiment B, 13100 Aix-en-Provence, France

[a)]Author to whom correspondence should be addressed: umberto.morbbiducci@polito.it

ABSTRACT

This study reports the first biomedical application of event-based imaging velocimetry (EBIV) and demonstrates its feasibility for investigating cardiac hemodynamics. Experiments were conducted in a left-heart pulse duplicator to characterize intraventricular fluid mechanics with a transcatheter mitral valve. EBIV and conventional particle image velocimetry (PIV) measurements were acquired synchronously under two distinct flow regimes. The aim was to assess whether EBIV—a neuromorphic, event-driven imaging technology—can provide flow measurements comparable to those obtained with PIV, which serves as the reference technique for the *in vitro* assessment of prosthetic heart valves hydrodynamics. The results show that EBIV accurately reproduces valve-related hemodynamic features, including phase-averaged velocity fields, vortex structures, circulation, Lagrangian trajectories, and pulsatile kinetic energy, while producing markedly compact datasets and benefiting from an extended dynamic range. A modal analysis based on proper orthogonal decomposition further confirms a strong agreement between EBIV and PIV, revealing nearly identical dominant spatial modes. These findings establish EBIV as a promising, data-efficient, and real-time capable alternative for the quantitative characterization of cardiac flows. This first biomedical application underscores EBIV's potential for device assessment, intraventricular flow analysis, and broader application in experimental cardiovascular research.

I. INTRODUCTION

In vitro fluid mechanics techniques historically played a crucial role in advancing the understanding of cardiovascular flows, providing fundamental insights into their underlying physics. These experimental approaches remain pivotal for the design, optimization, and characterization of cardiovascular devices—particularly prosthetic heart valves (PHVs).[1–5] Specifically, *in vitro* investigations, both in terms of qualitative flow visualizations or more quantitative analyses, are essential to characterize features such as jet flows, regions of separation and recirculation, vortex structures, shear layers, or quantify turbulence, which are critical determinants of device performance and implantation success.

In the context of heart valve prostheses, the impact of their design features on the hemodynamics of the left ventricle (LV) should be carefully evaluated. From a biofluid-dynamics perspective, the LV is a dynamic chamber whose filling and ejection phases are dominated by coherent vortex structures. In healthy subjects, a ring-shaped vortex forms near the mitral valve leaflets during diastolic filling because of the jet of blood incoming from the left atrium. This physiological vortex helps guide blood into the ventricle promoting effective filling, facilitating a smooth transition to the systolic ejection phase, and helping prevent blood clot formation.[6–9] This vortex structure travels toward the ventricular apex, interacts with ventricle walls, and is redirected toward the outflow tract to be ejected in aorta, minimizing energy dissipation.[10] Disruptions to this flow organization—whether due to pathology or to mitral PHVs that fail to replicate native behavior—have been linked to increased viscous losses, impaired LV chamber washout, and elevated myocardial workload.[11–14] These findings have motivated the design of mitral valve prostheses that aim to restore physiological intraventricular flow patterns as closely as possible.

Among *in vitro* experimental techniques, particle image velocimetry (PIV) has long been regarded as the reference standard for evaluating blood-recirculating devices, owing to its accuracy, robustness, and well-established processing frameworks.[13,14] PIV is routinely employed as a benchmark for numerical simulations, and international standards such as BS EN ISO 5840 recommend PIV-based flow

measurements to assess thrombogenic and hemolytic potential in PHVs, thereby supporting regulatory approval.[15,16] Despite its advantages, PIV is inherently limited by the frame-rate constraints of conventional cameras, the large data volumes generated, and the need for complex and costly optical setups.

While numerous studies have applied PIV to examine the fluid dynamics associated with aortic valve prostheses, considerably fewer have used PIV to analyze the impact of mitral valve prostheses on LV fluid dynamics. Understanding these flow fields remains challenging due to the inherent hemodynamic complexity and ventricular wall deformability. In the literature, two-dimensional PIV—either standard planar PIV (providing two velocity components) or stereoscopic (providing three velocity components)—is the most used to characterize LV flow patterns.[17–24] More advanced configurations, such as tomographic PIV and four-dimensional particle tracking velocimetry, have been used in a smaller number of studies to obtain volumetric measurements of intraventricular vortices.[1,25]

Recent advances in neuromorphic sensing have enabled the development of event-based imaging velocimetry (EBIV), an alternative approach that records pixel intensity changes asynchronously, rather than capturing full image frames at fixed time intervals. Event-based vision (EBV) sensors—also known as dynamic vision sensors (DVS)—implement an asynchronous, per-pixel detection of temporal contrast, whereby events are generated only in response to local intensity variations.[26–29] EBIV methods leverage these properties by accumulating events within temporal windows to produce *pseudo-images* that can be processed with standard correlation algorithms[30,31] or alternatively with particle tracking approaches.

This acquisition paradigm offers three main advantages for velocimetry: (i) high temporal fidelity at the pixel level, due to asynchronous event generation with microsecond latency, independent of global frame exposure, as each pixel reacts independently to local light intensity variations; (ii) intrinsic data sparsity, since static regions on the image (e.g., backgrounds) generate no events; and (iii) an extended dynamic range (DR), enabling simultaneous visualization of bright and dark regions typical of laser-based measurements. It is worth noting that the improved temporal fidelity of EBIV is not intrinsically tied to pulsed illumination. Event-based imaging velocimetry has been shown to operate effectively also under continuous-wave laser illumination, exploiting the intrinsic temporal resolution of event-based sensors to resolve particle motion without double-pulse synchronization.[30] This further emphasizes that the temporal fidelity of EBIV originates from the sensing paradigm itself, rather than from the illumination scheme.

Prior studies on canonical flows—such as jets and wakes—have demonstrated that EBIV accurately reproduces dominant fluid structures, reduces data bandwidth by one to three orders of magnitude compared with frame-based methods, and enables real-time or control-oriented applications.[28,30–32] Even though its low implementation cost, simplified setup, and capacity for time-resolved measurements make it particularly promising for this domain, EBIV has not yet been applied to cardiovascular flow visualization and quantification.

Despite its accuracy, the broad application of conventional PIV to cardiovascular flows remains constrained by high data rates, frame-based acquisition, and sensitivity to illumination conditions, which limit its applicability for extended, iterative, or real-time investigations in cardiac simulators. EBIV offers a complementary paradigm by asynchronously capturing only intensity changes associated with particle motion, resulting in substantially reduced data volumes, enhanced robustness to illumination heterogeneity, and improved temporal fidelity at the pixel level. In addition, EBIV relies on a more compact and cost-effective sensing hardware compared with high-end PIV imaging systems. Owing to its asynchronous acquisition paradigm and intrinsically sparse data output, EBIV significantly reduces data throughput, storage requirements, and computational overhead, while avoiding the need for high-frame-rate cameras and complex/costly measurement equipment. These characteristics facilitate its adoption in operationally demanding experimental settings, such as long-duration measurements, rapid screening of multiple operating conditions, or iterative device-testing workflows, where conventional frame-based PIV systems may become logistically and economically burdensome. These features make EBIV particularly attractive for *in vitro* cardiovascular applications where long-duration measurements, rapid testing of multiple operating conditions, or real-time flow assessment is desirable.

Building on these premises, the present study introduces the first application of EBIV to cardiac flows analysis conducting simultaneous, phase-locked EBIV and PIV measurements in a LV phantom housed within a pulse duplicator and equipped with a transcatheter mitral valve designed to reproduce nearly physiological hemodynamics. By adopting identical data-processing workflows—based on reconstructed pseudo-images for EBIV and acquired frame pairs for PIV—methodological consistency and direct comparability are ensured. The analysis focuses on biofluid-dynamic quantities of practical and clinical relevance, characterizing the performance of the prosthetic valve under two representative flow regimes. Within this framework, PIV serves as the established reference technique, while EBIV is evaluated as a data-efficient, high-dynamic range and economically attractive alternative for biomedical flow studies.

Accordingly, the value of EBIV in this study lies not in outperforming PIV, but in demonstrating comparable performance with a data-efficient, asynchronous acquisition paradigm that is well suited for operationally demanding cardiovascular experiments.

II. MATERIALS AND METHODS

A. Experimental setup

All experiments were performed using a left-heart pulse duplicator (ViVitro Pulse Duplicator, ViVitro Labs Inc.), a commercial customizable platform for the hydrodynamic assessment of cardiovascular devices compliant with the ISO 5840 standard. The system reproduces ventricular filling and ejection within a closed hydraulic loop and consists of two coupled circuits: (i) an upper flow circuit including the atrial, ventricular, and aortic chambers filled with the working fluid and (ii) a lower hydraulic circuit filled with distilled water, which drives the ventricular membrane through a pulsatile piston pump. The pulsatile pump generates volumetric changes in the hydraulic circuit, resulting in the expansion and contraction of the silicone left ventricle phantom (ViVitro Labs Inc.). A schematic representation of the test section is provided in Fig. 1. The LV phantom is immersed in a transparent octagonal plexiglass tank, custom designed to facilitate optical access and enable velocimetry measurements by providing multiple entry points for laser sheets and camera visualization. The pump was operated in velocity-control mode to reproduce a physiological

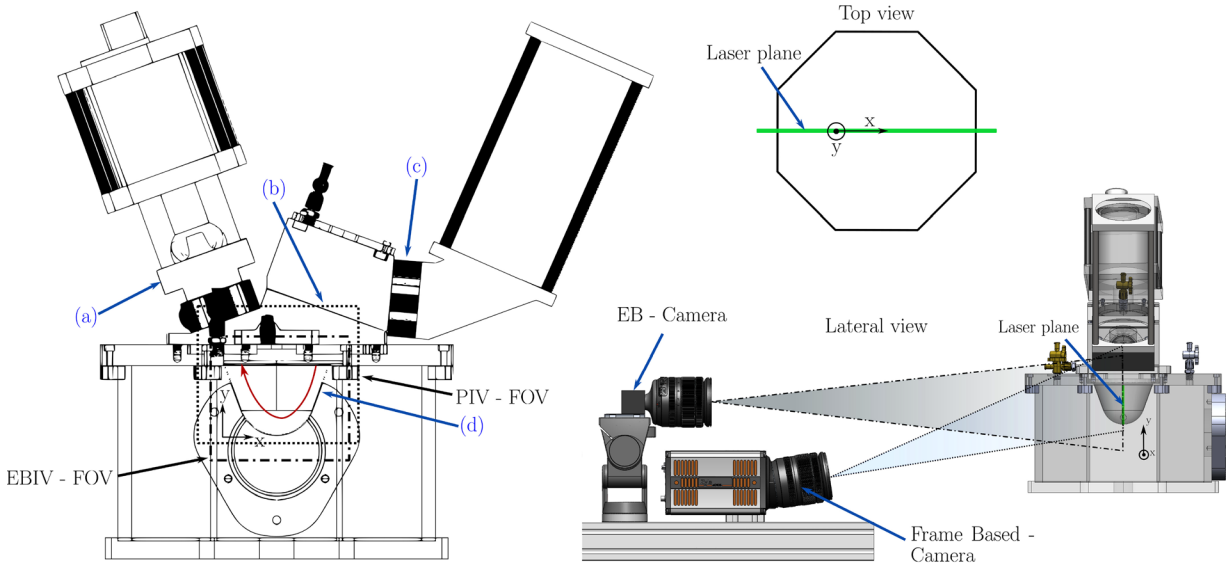

FIG. 1. Sketch of the test section reproducing the left-ventricle mock loop used in the *in vitro* experiments. Left (Frontal View): (a) aortic valve holder; (b) mitral valve holder; (c) electromagnetic flowmeter; and (d) transparent silicone left ventricle. EBIV (dash-dotted box) and PIV (dotted box) fields of view are overlaid on the measurement plane, highlighting the coverage and overlap used for co-registered analysis. The red arrow sketches the intraventricular flow path: inflow through the mitral valve, filling of the left ventricle, and outflow through the aortic valve. Bottom-Right (Lateral View): placement of the event-based (EB) and frame-based cameras with respect to the measurement plane (laser sheet). Top-Right (Top View): laser plane (green line) and the reference axes (x, y).

waveform at 70 bpm with a 35% systolic duration. Two cardiac-output (CO) conditions, 3.5 ($CO_{3.5}$) and 5.0 (CO_5) l min^{-1}, specified by the International Standard BS EN ISO 5840,[33] were tested. A saline solution (NaCl 0.9% w/v) was used as the working fluid, and neutrally buoyant tracer particles (polyamide, diameter 100 μm, density 1.1 g cm^{-3}; LaVision GmbH) were added for flow visualization. Although more complex blood-analogue fluids (e.g., water–glycerol mixtures) are commonly used to reproduce physiological rheology, a saline solution was selected here to ensure high optical transparency and measurement robustness, without affecting the direct one-to-one comparison between EBIV and PIV that constitutes the focus of this study.

A transcatheter mitral valve prosthetic model that will be presented below was mounted in the mitral position, while a no-leakage valve (ViVitro Labs Inc.) was installed in the aortic position.

During diastole, the fluid entered the transparent ventricle through the mitral valve from the atrial chamber, allowing optical access for laser illumination and camera imaging. During systole, the contraction of the ventricular phantom directed the flow through the aortic prosthesis into the aortic chamber. This chamber included an aortic root phantom and discharged back to the left atrial chamber via an adjustable peripheral resistance, enabling precise control of mean aortic pressure (here set to MAP = 100 mm Hg, according to the standard[33]). Flow rate was monitored using an electromagnetic flowmeter (Model 501, Carolina Medical Electronics) positioned upstream of the mitral valve plane. Pressures in the atrial chamber, ventricle, and downstream of the aortic valve were recorded using pressure transducers (Model 6069, Utah Medical Products).

The left-heart simulator was equipped with a Epygon transcatheter mitral valve (Affluent Medical SA) of a nominal diameter D of 42 mm (Fig. 2). Briefly, the Epygon valve was assembled using a single

FIG. 2. Epygon transcatheter mitral valve (Affluent Medical SA) featuring a single pericardial leaflet mounted on a D-shaped, self-expandable nitinol stent frame: (a) top view, (b) lateral view, and (c) bottom view.

pericardial leaflet mounted on a D-shaped, self-expandable nitinol stent frame.[34,35] The design of the valve is intended to promote near-physiological diastolic vortex formation within the LV, minimizing abnormal shear stresses and energy dissipation. The device is currently under clinical evaluation in the MINERVA first-in-human trial (ClinicalTrials.gov Identifier: NCT04775108).[36]

Representative pressure waveforms for the atrial, ventricular, and aortic chambers under the condition CO_5 are presented in Fig. 3, demonstrating the physiological timing of filling and ejection. The lower cardiac-output case ($CO_{3.5}$) exhibited a qualitatively similar temporal profile.

B. Optical system and cameras

EBIV and PIV measurements were conducted on the aortomitral plane to capture the main features of the intraventricular filling vortex and its dynamic evolution toward the outflow tract (see Fig. 1). The measurement plane was illuminated using a dual-cavity Nd:YAG laser (Dantec Dynamics, maximum repetition rate: 15 Hz, maximum power

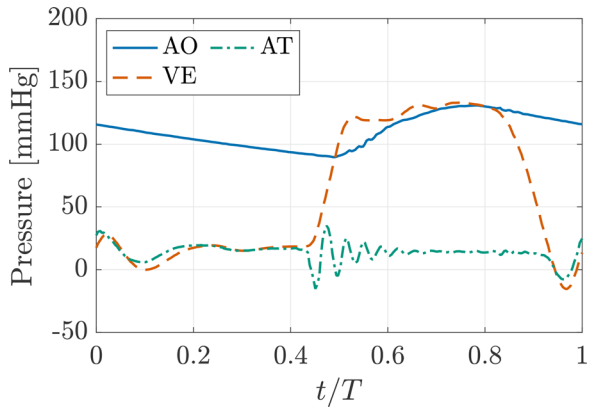

FIG. 3. Measured pressure waveforms at atrial (AT), ventricular (VE), and aortic (AO) locations for the CO_5 condition, ensemble-averaged over 10 consecutive cardiac cycles.

per pulse: 200 mJ/pulse), shaped into a light sheet of approximately 1 mm thickness. Image acquisition was performed simultaneously using two cameras arranged in a vertically stacked configuration, with one camera positioned above the other: (i, top) a Prophesee EVK-4 event-based camera equipped with a Sony IMX636 sensor (full resolution: $1280 \times 720\ px^2$) and (ii, bottom) an Andor Zyla 5.5 scientific CMOS (sCMOS) camera (full resolution: $2560 \times 2160\ px^2$). Both cameras were fitted with Zeiss Milvus 50 mm f/2.0 lenses. Additionally, the sCMOS camera was equipped with a 532 nm bandpass filter to isolate the laser wavelength and improve image quality. The aperture settings ($f_\#$) were f/8 for the event-based camera and to f/9.5 (corresponding to the half-stop between the f/8 and f/11 on the lens barrel) for the sCMOS system.

Since the frame-based sCMOS camera was positioned below the event-based camera, it viewed the measurement plane at a slightly different vertical angle. To ensure uniform focusing across the illuminated region, the sCMOS camera was mounted on a Scheimpflug adapter, maintaining optical coplanarity between the sensor and the light sheet. Finally, the event-based camera, which is equipped with a smaller physical sensor, would otherwise have captured a reduced field of view if positioned at the same distance as the sCMOS camera. Therefore, to achieve comparable spatial coverage of the ventricular plane, the event-based camera was placed slightly farther from the test chamber, ensuring that both imaging systems recorded overlapping regions of interest (ROI).

A distinctive feature of event-based imaging is its adjustable sensor bias configuration, which governs both the detection threshold and the temporal response. For velocimetry applications, only positive events—corresponding to increases in light intensity—are typically retained, while negative events are discarded to maximize the effective bandwidth and suppress spurious detections. In the present study, the internal bias parameters of the event-based camera were independently tuned separately for each cardiac-output condition to optimize event density and signal fidelity (Table I).

C. Triggering and phase locking

The pulse duplicator generated a transistor–transistor logic (TTL) reference signal each time the piston-driven waveform crossed zero on the downstroke. This signal was fed to a hardware synchronizer (Performance Synchronizer, Dantec Dynamics), which issued synchronized triggers to both the laser and cameras for dual-pulse acquisition. A programmable electronic delay between the duplicator's TTL signal and the trigger emission enabled precise selection of the acquisition phase within the cardiac cycle. A schematic of the acquisition and synchronization sequence is provided in Fig. 4. In this study, the reference phase was set at the peak of the E-wave, corresponding to the early diastolic filling through the mitral valve (Fig. 5).

TABLE I. EBIV bias settings for the two cardiac outputs.

Bias parameter	CO 5.0 l/min	CO 3.5 l/min
Diff-OFF	190	190
Diff-ON	92	−25
High-pass filter	120	110
FO	−10	−35
Refractory period	−20	−20

Acquisitions were performed at 14 Hz, with an inter-pulse delay of 1000 μs, while the duplicator operated at 70 bpm (cardiac frequency: $f_{heart} \approx 1.167$ Hz). The corresponding cardiac period ($T \approx 0.857$ s) was thus evenly divided into 12 samples per cycle, providing twelve uniformly spaced phase-locked instants (ϕ). For each operating condition, 250 frame pairs were acquired at each phase, ensuring statistical convergence for ensemble averaging. Figure 5 displays the instantaneous flow rate upstream of the mitral valve for the CO_5 working condition, where the time points corresponding to the twelve acquisition phases used in the phase-locked analysis are highlighted. The lower cardiac-output working condition $CO_{3.5}$ exhibited a similar temporal pattern.

Geometric calibration was performed using a planar target ($30 \times 25\ mm^2$) featuring a 1 mm high-contrast grid (dark lines on a light background) positioned on the measurement plane. Images from both cameras were mapped onto a common reference frame using a homography-based alignment procedure. The homography procedure employed for cross-modality alignment is described in detail in Subsection II E.

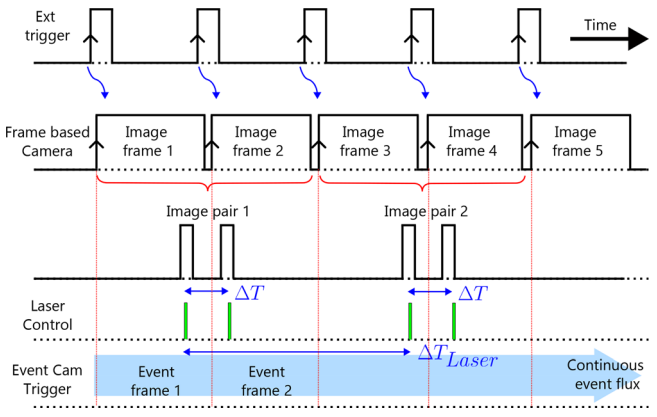

FIG. 4. Timing diagram of the acquisition system, showing synchronized triggers for the laser, event-based camera, and frame-based camera for PIV measurements.

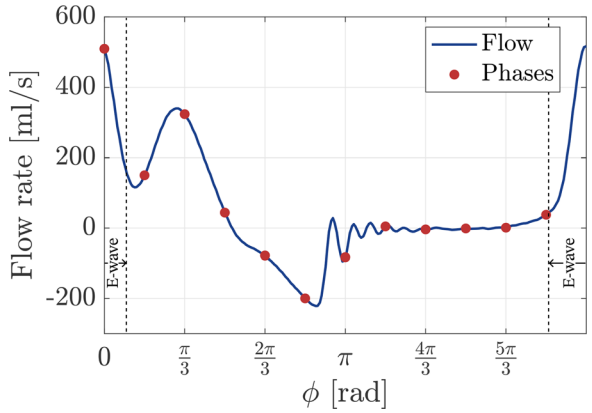

FIG. 5. Flow rate upstream of the mitral valve for the CO_5 condition. The markers indicate the temporal positions of the twelve uniformly spaced acquisition phases used in the phase-locked analysis. E-wave peak at $\phi = 0$ rad.

D. EBIV data processing

EBV sensors rely on an asynchronous acquisition mechanism that detects temporal contrast at the pixel level. Specifically, each pixel generates an event when the temporal derivative of the logarithmic light intensity (I) exceeds a predefined threshold:

$$C_{\text{temporal}} = \frac{\mathrm{d}}{\mathrm{d}t} \ln(I(t)), \tag{1}$$

thus responding exclusively to temporal changes in the scene.[26–28] Unlike conventional frame-based cameras that deliver images at fixed intervals, EBV sensors produce a continuous stream of time-stamped events. Each event carries a pixel address, a microsecond-scale time-stamp, and a polarity (on for positive, off for negative), representing only intensity variations.[29]

The sensor employed here (Sony-Prophesee IMX636) provides a nominal dynamic range of ∼120 dB (≈ 20 effective bits at 6 dB per bit),[37] markedly exceeding the ∼60–70 dB (10–12 bits) typical of high-speed cameras and the ∼96 dB (16 bits) achievable with advanced sCMOS devices.[29,38]

For velocimetry, this event stream must be reformatted into structures compatible with correlation-based algorithms. The adopted approach follows the pulsed-EBIV principle.[31] As illustrated in Fig. 4, in this study, the frame-based camera signal defined the temporal window used for pseudo-frame reconstruction, thereby avoiding synchronization issues related to sensor latency. Events generated by light scattering from tracer particles were thus clustered and associated with a unique pulse, effectively "freezing" the particle positions at discrete instants in time. Figure 6(a) shows the histogram of two consecutive positive triggers detected by the event-based camera, with the event distribution aligning closely with the laser signal and exhibiting two distinct peaks corresponding to the dual-pulse illumination.

An example of the probability density function (PDF) of the total number of events detected between two consecutive positive triggers is reported in Fig. 6(b): the sharply concentrated distribution demonstrates the temporal stability of the sensor response to pulsed illumination, ensuring that the information density in each pseudo-image remains consistent-an essential condition for robust cross-correlation analysis.

During acquisition, the mean event rate was $[2.33 \pm 0.7] \times 10^3$ events s^{-1}, as obtained from the bias configuration summarized in Table I. This value is lower than those typically reported in the literature,[28,31] mainly because only a portion of the field of view (i.e., the LV volume) was seeded. Additionally, the "bias-on" parameter introduced before was limited to prevent excessive event rates due to laser reflections from the ventricular walls.

From the accumulated events, pseudo-images were reconstructed by assigning unit intensity to all pixels that registered an event within the laser pulse interval, producing dense binary maps of tracer locations. To enhance correlation robustness, pseudo-images were smoothed with a Gaussian kernel whose size was optimized through a comparative analysis: Fig. 7(a) presents the PDF of the particle-equivalent diameters in the raw pseudo-frames and after Gaussian filtering with two distinct kernel size (k_g) values, $3 \times 3\,\text{px}^2$ ($k_g 3$) and $5 \times 5\,\text{px}^2$ ($k_g 5$), respectively. Each pseudo-image was first binarized through thresholding, and individual connected regions were isolated to compute the diameter of a circle having the same area as the region.

The Gaussian filtering applied to the EBIV pseudo-images does not serve to increase the intrinsic spatial resolution of the

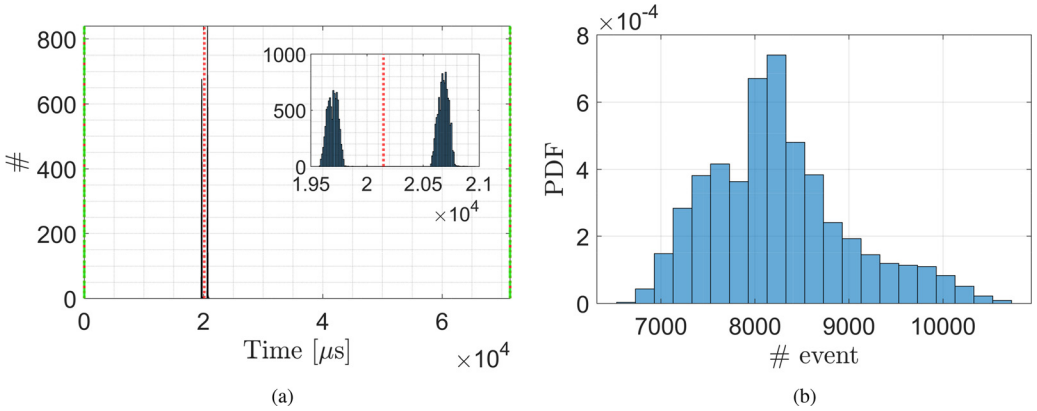

(a) (b)

FIG. 6. (a) Histogram of two consecutive positive triggers detected by the event-based camera. (b) PDF of the total number of events between two consecutive positive triggers detected by the event-based camera.

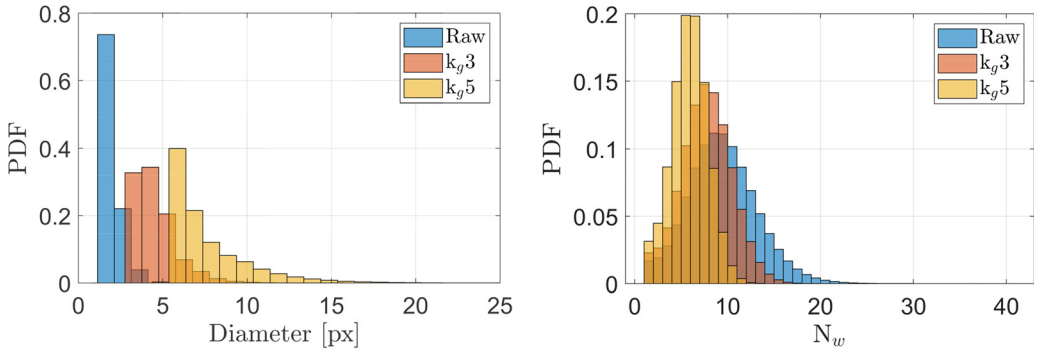

FIG. 7. (a) PDF of the particle-equivalent diameter detected in EBIV pseudo-frames; (b) PDF of the number of detected particle images per interrogation window, N_w (window 40×40 px^2, 75% overlap). Both panels use the same legend: before (raw, in blue) and after Gaussian smoothing with $k_g = 3 \times 3$ px^2 (k_g3, in red) and $k_g = 5 \times 5$ px^2 (k_g5, in yellow).

measurement, but serves to stabilize the cross-correlation process by shaping event clusters into smooth particle-like intensity distributions. This procedure is conceptually analogous to particle image formation in conventional PIV, where optical blur and pre-processing define an effective particle size optimized for correlation robustness. The smaller kernel effectively suppressed high-frequency noise, eliminating the spurious peak near px $= 1$ in the raw data while preserving a mean particle diameter of $\approx$5 px—consistent with the reference PIV dataset. Comparable filtering parameters have been reported in EBIV literature as optimal for reproducing the Gaussian intensity profile of PIV tracers and stabilizing correlation peaks.[30–32] In all these works, small Gaussian kernels (typically $k_g \leq 3 \times 3$ px^2) or subpixel standard deviations ($\sigma \approx 0.5$–1 px) were found to provide the best balance between particle compactness and correlation reliability.

Figure 7(b) shows the PDF of the number of detected particle images per interrogation window (N_w) computed using a 40×40 pixels^2 window with 75% overlap. The parameter N_w represents the local seeding density and directly determines the reliability of the cross-correlation process. According to the classical literature on PIV,[39] an average occupancy of approximately 10 particles per interrogation window ensures an optimal signal-to-noise ratio (SNR) in the correlation peak while avoiding pattern overlap and loss of correlation associated with the three-dimensionality of the flow. Similar seeding conditions have been shown to yield stable and accurate flow reconstructions in event-based velocimetry.[30–32] In agreement with these established criteria, the present results obtained with a Gaussian kernel size of $k_g = 3 \times 3$ px^2 maintain N_w within the recommended range, providing the best compromise between noise suppression, accurate particle size representation, and statistically robust correlation conditions.

The resulting sequence of pseudo-images preserves the temporal cadence of the laser pulses and is fully compatible with standard cross-correlation algorithms.

This approach leverages the intrinsic temporal resolution of event-based cameras while minimizing redundancy: static regions generate no events, and only dynamically illuminated particles contribute to the pseudo-image. The resulting datasets are therefore significantly smaller in bandwidth than those from high-speed imaging but retain sufficient information for full-field velocity reconstruction.[32] Moreover, by synchronizing event accumulation with pulsed illumination, latency and jitter effects typical of EBIV sensors are effectively mitigated, as events are unambiguously linked to distinct trigger times.[31]

E. Image processing and vector computation

To enable a direct comparison between the two measurement techniques, PIV images were mapped onto the EBIV reference frame by means of a projective transformation (see Fig. 8).

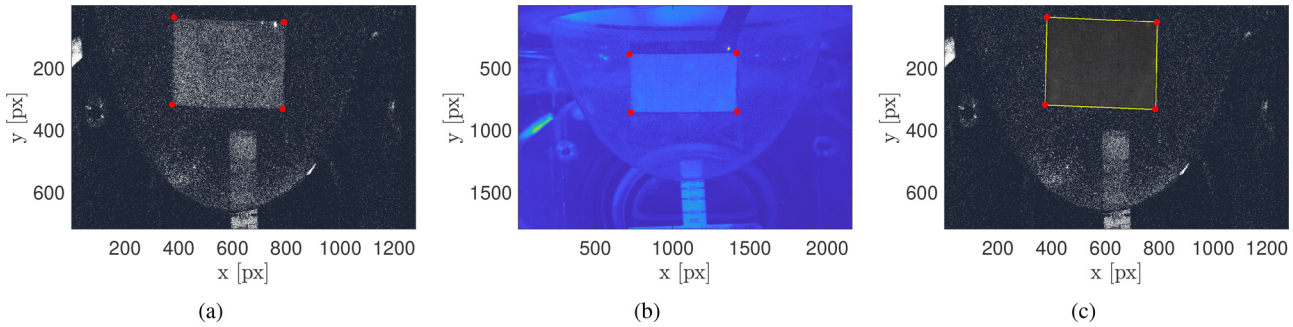

FIG. 8. Planar projective co-registration between PIV and EBIV. (a) EBIV view with the four red calibration markers defining the reference frame. (b) PIV view with the same markers, used to estimate the homography $\mathbf{H}$ between the two image planes. (c) EBIV image overlaid with the PIV calibration target warped by $\mathbf{H}$ (yellow shape) after bilinear resampling.

A planar calibration target was placed in the measurement plane, and corresponding reference points were identified in both camera views. From these points $\{\mathbf{p}_i^A\}$ for the EBIV camera (reference) and $\{\mathbf{p}_i^B\}$ for the PIV camera (to be mapped), expressed in homogeneous coordinates, the homography matrix $\mathbf{H} \in \mathbb{R}^{3\times3}$ was estimated such that

$$\mathbf{p}_i^A \sim \mathbf{H}\,\mathbf{p}_i^B. \tag{2}$$

The quality of the transformation was verified by overlaying the warped PIV calibration image onto the EBIV view and inspecting the alignment of reference markers and field boundaries across the region of interest. The transformation was validated using 20 control points located along the calibration target edges, yielding a mean squared error of 0.967 px. Once validated, the same transformation was applied to all PIV frames. The resampled PIV images were obtained according to

$$\tilde{I}_{\mathrm{B}\to\mathrm{A}}(\mathbf{x}) = I_{\mathrm{B}}(\mathbf{H}^{-1}\mathbf{x}), \tag{3}$$

where I_{B} denotes the PIV image intensity field and $\tilde{I}_{\mathrm{B}\to\mathrm{A}}$ its projection onto the EBIV coordinate frame, while $\mathbf{x}$ is the spatial coordinate vector in the EBIV image plane. The images were resampled by bilinear interpolation, ensuring subpixel accuracy and preventing aliasing. This procedure yielded strict spatial co-registration between the two techniques, providing a consistent basis for subsequent comparative analysis.

Velocity fields for both EBIV and PIV datasets were computed using the PaIRS-UniNa software suite.[40–47] A multi-pass cross-correlation algorithm with progressive refinement of the interrogation windows was employed. The final pass used $32 \times 32\,\mathrm{px}^2$ interrogation windows with 50% overlap.

The native image resolutions were $22.8\,\mathrm{px\,mm^{-1}}$ for the PIV camera and $13.73\,\mathrm{px\,mm^{-1}}$ for the EBIV camera. After the PIV images were mapped onto the EBIV reference frame, both datasets shared the same effective resolution of $13.73\,\mathrm{px\,mm^{-1}}$, which was adopted for all further analyses. With 50% overlap, the resulting vector pitch was $p = (1 - 0.50) \times 32 = 16\,\mathrm{px}$, corresponding to a physical spacing, normalized with respect to the mitral valve's diameter, of $\sim 2.8 \times 10^{-2}$. This yielded an effective vector density of approximately $0.85\,\mathrm{vectors\,mm^{-1}}$ across the field of view. The computed fields provided the in-plane velocity components $u(x, y)$ and $v(x, y)$ on the aortomitral plane, representing the horizontal and vertical components of the instantaneous velocity vector, respectively (Fig. 1).

F. Fluid mechanics quantities

This subsection introduces the fluid mechanics quantities employed to compare the EBIV and PIV measurements. Unless otherwise specified, all computations were performed on the phase-mean velocity fields restricted to the phase-specific domain $\mathscr{D}^{(\phi)}$. Each phase-specific domain was obtained by averaging and regularizing the instantaneous binary masks derived from the cross-correlation maps, thereby defining a consistent ventricular cavity region for each phase of the cardiac cycle.

From the measured in-plane velocity field $\mathbf{u}(x, y) = (u, v)$,the out-of-plane vorticity can be computed as:

$$\omega_z = (\nabla \times \mathbf{u})_z = \frac{\partial v}{\partial x} - \frac{\partial u}{\partial y}, \tag{4}$$

which foregrounds the presence of shear layers and coherent vortical structures relevant to intraventricular transport. In the LV, both the sign and spatial distribution of ω_z reflect the orientation and persistence of the diastolic vortex, a key mechanism for flow redirection toward the outflow tract.

The velocity gradient tensor is defined as:

$$\nabla\mathbf{u} = \begin{bmatrix} \dfrac{\partial u}{\partial x} & \dfrac{\partial u}{\partial y} \\ \dfrac{\partial v}{\partial x} & \dfrac{\partial v}{\partial y} \end{bmatrix}, \tag{5}$$

and can be decomposed into its symmetric (strain rate) and antisymmetric (rotation) components

$$\mathbf{S} = \frac{1}{2}(\nabla\mathbf{u} + \nabla\mathbf{u}^\top), \qquad \Omega = \frac{1}{2}(\nabla\mathbf{u} - \nabla\mathbf{u}^\top). \tag{6}$$

The individual components of the strain rate tensor $\mathbf{S}$ and the rotation tensor Ω that can be computed from the measured velocity vector $\mathbf{u}(x, y)$ are therefore

$$S_{xx} = \frac{\partial u}{\partial x}, \quad S_{yy} = \frac{\partial v}{\partial y}, \quad S_{xy} = S_{yx} = \frac{1}{2}\left(\frac{\partial u}{\partial y} + \frac{\partial v}{\partial x}\right), \tag{7}$$

$$\Omega_{xy} = -\Omega_{yx} = \frac{1}{2}\left(\frac{\partial u}{\partial y} - \frac{\partial v}{\partial x}\right). \tag{8}$$

Notably, the quantity $2\Omega_{xy} = \frac{\partial u}{\partial y} - \frac{\partial v}{\partial x} = -\omega_z$ establishes the direct link between the antisymmetric component of the velocity gradient and the local out-of-plane vorticity.

A scalar measure of local deformation is given by the strain rate magnitude, defined as:

$$|S| = \sqrt{2(S_{xx}^2 + S_{yy}^2 + 2S_{xy}^2)}. \tag{9}$$

The λ_2 criterion[48] was applied to identify vortex cores, corresponding to regions where the second-largest eigenvalue of the symmetric tensor $\mathbf{M} = \mathbf{S}^2 + \Omega^2$ is negative. Because λ_2 balances rotation against strain, it suppresses spurious detections in high-shear regions and isolates compact, dynamically relevant vortex structures. This makes it more physiologically relevant than vorticity magnitude alone, which can also peak in pure shear layers without a coherent vortex core.

To condense the phase-resolved dynamics into scalar trends, two integral quantities over the refined domains $\mathscr{D}^{(\phi)}$ were evaluated. The *circulation per unit area*, which quantifies the net rotational content of the fluid, is defined by Stokes theorem as:

$$\langle\Gamma\rangle(\phi) = \frac{1}{A(\phi)}\int_{\mathscr{D}(\phi)} \omega_z(\phi)\,\mathrm{d}A(\phi), \tag{10}$$

where (ϕ) denotes the area of the phase-specific domain. With the standard coordinate orientation (x rightward, y upward, Figs. 1 and 8), the sign of Γ indicates the rotation direction of vortex structures ($\Gamma > 0$ counterclockwise rotation, $\Gamma < 0$ clockwise rotation), while values near zero indicate the existence of weak rotation or nearly balanced rotation of counter-rotating vortices.

To analyze energetic trends, the triple decomposition framework[49,50] was adopted. Let the instantaneous in-plane velocity be $\mathbf{u}(x, y, t) = (u, v)$, the cycle-mean field be $\overline{\mathbf{u}}(x, y) = (\overline{u}, \overline{v})$, and $\mathbf{u}_{\mathrm{mean}}^{(\phi)}(x, y)$ the phase-conditioned mean built from 250 realizations at phase ϕ. The instantaneous velocity can be decomposed as:

$$\mathbf{u} = \overline{\mathbf{u}} + \underbrace{\left(\mathbf{u}_{\text{mean}}^{(\phi)} - \overline{\mathbf{u}}\right)}_{\text{phase-locked component } \tilde{\mathbf{u}}^{(\phi)}} + \underbrace{\left(\mathbf{u} - \mathbf{u}_{\text{mean}}^{(\phi)}\right)}_{\text{residual } \mathbf{u}'}, \tag{11}$$

where $\tilde{\mathbf{u}}^{(\phi)}$ represents the coherent, cycle-synchronous fluctuations associated with the periodic cardiac motion, while $\mathbf{u}'$ denotes the residual (stochastic) fluctuations within each phase.

From this decomposition, the *phase-locked (pulsatile) kinetic energy* (PKE) at each phase ϕ is defined as:

$$\text{PKE}^{(\phi)}(x,y) = \frac{1}{2}\rho\left[(u_{\text{mean}}^{(\phi)} - \overline{u})^2 + (v_{\text{mean}}^{(\phi)} - \overline{v})^2\right], \tag{12}$$

where ρ is the fluid density. The PKE quantifies the energy associated with coherent, periodic fluctuations of the flow field relative to the cycle phase-conditioned mean velocity, thereby representing the kinetic contribution of the pulsatile component of motion dominant during ventricular filling and ejection. Although the total kinetic energy (KE) can be formally decomposed as:

$$\text{KE} = \overline{\frac{1}{2}\rho|\mathbf{u}|^2} = \frac{1}{2}\rho|\overline{\mathbf{u}}|^2 + \overline{\text{PKE}^{(\phi)}} + \overline{\text{TKE}}, \tag{13}$$

where TKE denotes the turbulent (residual) kinetic energy, the present analysis focuses exclusively on the phase-locked (pulsatile) component. This quantity encases periodic energy exchanges driving intraventricular vortex dynamics and provides a compact, scalar measure of the strength of coherent fluid structures throughout the cardiac cycle.

To ensure quantitative consistency across datasets and tested cardiac-output conditions, all computed quantities were expressed in dimensionless form adopting a statistically robust reference scale derived from the flow field data. The dimensionless procedure was designed to minimize the influence of outliers and inter-dataset variability while preserving the physical meaning of the underlying quantities.

Technically, with $N_\phi = 12$ equally spaced phases per cardiac cycle, a reference subset of phases was defined as:

$$\phi_{\text{ref}} = \{\phi_1, \phi_2, \phi_{12}\} = \left\{0, \frac{\pi}{6}, \frac{11\pi}{6}\right\}, \tag{14}$$

corresponding to the temporal window surrounding the E-wave peak (Fig. 5), which captures the interval of maximum diastolic inflow and the subsequent transition toward early flow deceleration. For each phase $\phi \in \phi_{\text{ref}}$, all instantaneous samples of the velocity magnitude $|\mathbf{u}|$ within the in-mask region were collected from both modalities (EBIV and PIV) and across all conditions. A single reference velocity was then obtained as the 95th percentile of the pooled distribution

$$\mathbf{U}_{\text{ref}}^{\text{pool}} = \text{Q}_{95}(|\mathbf{u}|(\phi_{\text{ref}})), \tag{15}$$

where $\text{Q}_{95}(\cdot)$ denotes the empirical 95th percentile operator. This reference velocity, which represents a robust characteristic velocity of the valve-opening phase, was used to define the nondimensional velocity magnitude

$$|\mathbf{u}|^* = \frac{|\mathbf{u}|}{\mathbf{U}_{\text{ref}}^{\text{pool}}}. \tag{16}$$

The phase-locked kinetic energy (PKE) was similarly normalized by the corresponding dynamic-pressure scale associated with $U_{\text{ref}}^{\text{pool}}$, yielding

$$\text{PKE}^* = \frac{\text{PKE}}{\frac{1}{2}\rho\,(\mathbf{U}_{\text{ref}}^{\text{pool}})^2}. \tag{17}$$

To ensure consistent visualization and comparison of coherent structures, λ_2 fields for vortex core identification were expressed in nondimensional form as:

$$\lambda_2^* = \frac{\lambda_2}{S_\lambda^{\text{pool}}}, \quad S_\lambda^{\text{pool}} = \text{Q}_{95}(|\lambda_2|(\phi_{\text{ref}})), \tag{18}$$

where S_λ^{pool} denotes a global vortex-intensity scale computed as the 95th percentile of $|\lambda_2|$ within the in-mask regions of the reference phases, pooled across all datasets. The introduced unified normalization framework guarantees cross-modality comparability and dynamic-range consistency while retaining the physical interpretability of each dimensionless field.

1. Proper orthogonal decomposition framework and derived metrics

To complement the analysis, *Proper Orthogonal Decomposition* (POD) was applied to the measured flow fields to extract the dominant coherent structures. POD provides an optimal, energy-ranked orthogonal basis that represents the flow field with minimal residual velocity variance for a given number of modes. Each mode identifies a spatial pattern that maximally contributes to the total kinetic energy content, offering a compact and physically interpretable description of large-scale flow organization.[51–55] POD-based modal analysis has already been applied—also to cardiovascular flows—to isolate coherent vortical structures and to identify reduced-order representations of complex dynamics in fluid motion.[53–55]

In this study, two complementary quantities were adopted to compare the modal representations extracted from EBIV and PIV, the modal assurance criterion (MAC), and the cumulative explained variance (CEV).

Technically, MAC quantifies the spatial correlation between pairs of POD modes obtained from different datasets, providing a scalar measure of their similarity. It is defined as:

$$\text{MAC}_{ij} = \frac{|\langle \boldsymbol{\psi}_i^{(\text{EBIV})}, \boldsymbol{\psi}_j^{(\text{PIV})} \rangle|^2}{\langle \boldsymbol{\psi}_i^{(\text{EBIV})}, \boldsymbol{\psi}_i^{(\text{EBIV})} \rangle \langle \boldsymbol{\psi}_j^{(\text{PIV})}, \boldsymbol{\psi}_j^{(\text{PIV})} \rangle}, \tag{19}$$

where $\boldsymbol{\psi}_i^{(\text{EBIV})}$ and $\boldsymbol{\psi}_j^{(\text{PIV})}$ denote the i-th and j-th POD modes from the EBIV and PIV datasets, respectively. Since POD modes are orthonormal, in Eq. (19), the normalization terms at the denominator are unity. A MAC value of 1 indicates identical modal shapes, while a value of 0 corresponds to orthogonal (uncorrelated) modes.

CEV quantifies how the total velocity variance (i.e., kinetic energy) is distributed among the modes. It is computed as:

$$\text{CEV}(n) = \frac{\sum_{k=1}^{n} \sigma_k^2}{\sum_{k=1}^{N} \sigma_{k,\text{PIV}}^2}, \tag{20}$$

where σ_k is the eigenvalue associated with the k-th POD mode ($k = 1, \ldots, N$) and the denominator is fixed and relative to PIV data. This normalization in Eq. (20) ensures that the EBIV and PIV cumulative curves are compared against a common energetic reference, highlighting whether EBIV captures a comparable fraction of the kinetic energy resolved by PIV measurement.

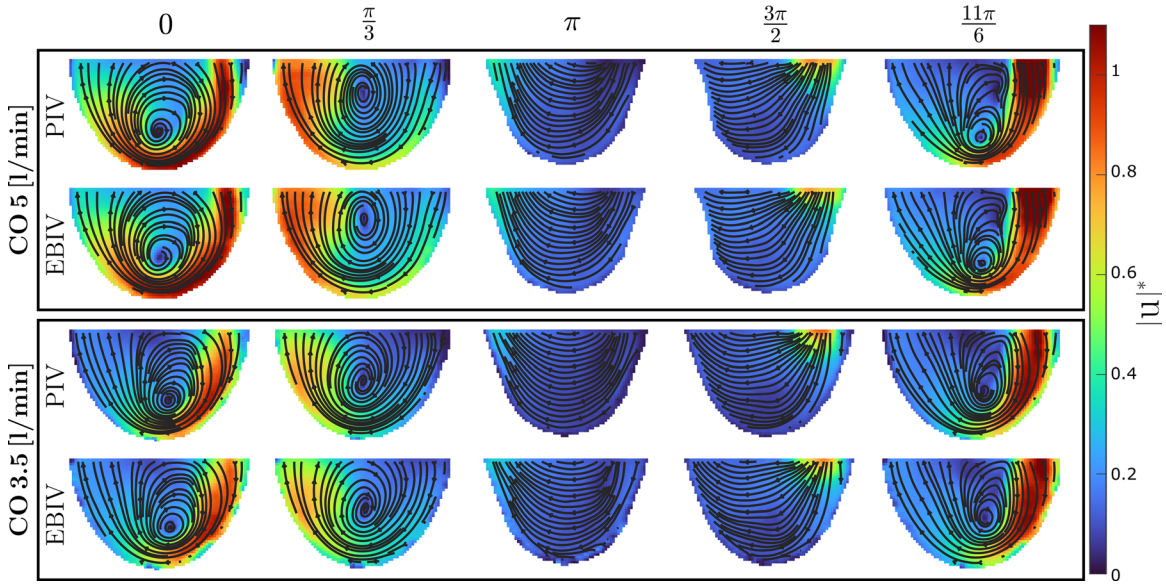

FIG. 9. Normalized velocity magnitude $|\mathbf{u}|^*$ with streamlines for representative diastolic phases. Rows (top to bottom): EBIV (CO_5), PIV (CO_5), EBIV ($CO_{3.5}$), and PIV ($CO_{3.5}$).

The POD analysis was applied to the phase-resolved velocity fields acquired from both EBIV and PIV at the two tested cardiac outputs, enabling a systematic comparison of the coherent structures and modal energy content across modalities.

III. RESULTS

A. Velocity and vorticity in the left ventricle

The evolution of the normalized velocity magnitude and vortex cores across the most representative phases of the diastolic filling is shown in Figs. 9 and 10, respectively. During early acceleration (around $\phi \simeq 11\pi/6$), a compact high-speed lobe appears immediately below the mitral plane and aligned with the inflow direction. At the same time, a coherent swirl develops within the apical half of the cavity (Fig. 9). As the phase advances toward mid-diastole (around $\phi \simeq \pi/3$), the high-speed region broadens and weakens, while velocity streamlines wrap around the forming vortex. During isovolumetric relaxation (around $\phi \simeq \pi$), both valves are closed and only minimal motion persists. Across cardiac outputs, CO_5 exhibits a stronger and

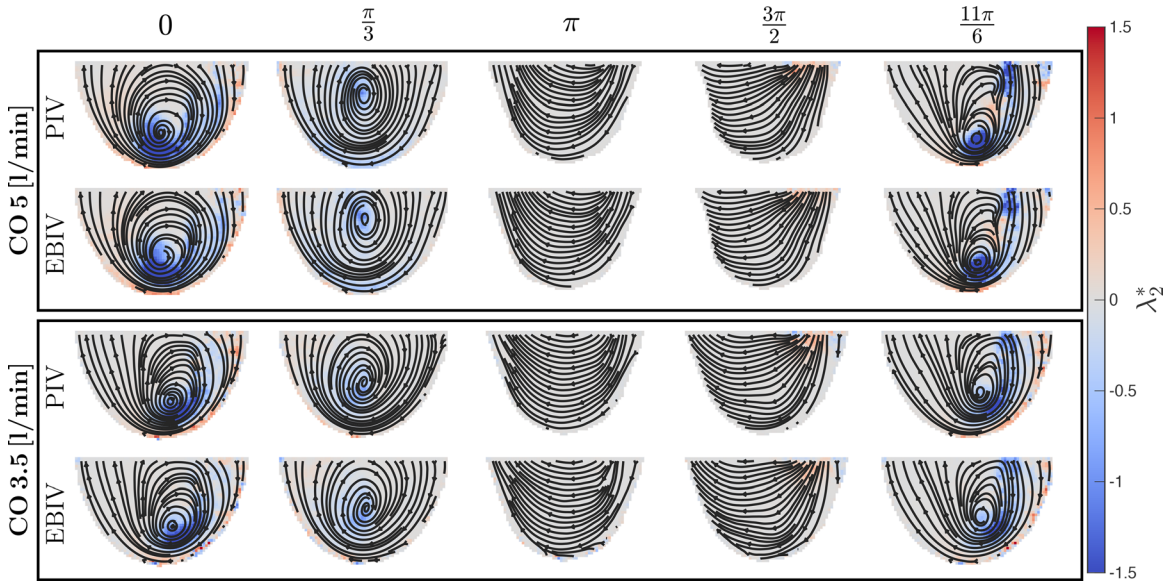

FIG. 10. Normalized λ_2^* maps with streamlines. Negative regions delineate the diastolic vortex core. Rows (top to bottom): EBIV (CO_5), PIV (CO_5), EBIV ($CO_{3.5}$), and PIV ($CO_{3.5}$).

more extended velocity core during early filling (in the range of $11\pi/6 \leq \phi \leq 0$) and a clearer late near-valvular speed-up, whereas $CO_{3.5}$ shows lower amplitudes and a more compact high-speed footprint. EBIV and PIV agree closely on the jet trajectory, penetration depth, and the location of the low-speed recirculating pocket near the apex. Locally, EBIV maps exhibit smoother color transitions along the edges of the high-speed lobe and across shear layers, while PIV maps display slightly sharper gradients near impingement and near-wall turning regions. These observed differences are confined to local gradient rendering and do not affect the large-scale topology, which remains consistent between modalities and flow conditions.

Negative λ_2^* regions delineate the diastolic vortex core (Fig. 10). In all cases, a compact negative pocket is visible during early-to-mid diastole (in the range of $11\pi/6 \leq \phi \leq \pi/3$) within the apical half of the ventricle, surrounded by closed streamlines. As diastole progresses, the vortex core drifts, reshapes, and expands while the outer spiral structure grows, before reconfiguring near the mitral plane during late filling. Increasing cardiac output enhances both the magnitude and spatial extent of the negative λ_2^* region, consistent with stronger shear and a more pronounced vortex roll-up at CO_5. The EBIV-PIV comparison demonstrates excellent agreement in the location of the vortex core, extent of the negative λ_2^* envelope, and global topology of the intraventricular vortex. EBIV maps tend to display smoother, less speckled negative patches around the core, whereas PIV occasionally exhibits localized sharper minima near the jet shear layer. Nevertheless, the overall vortex organization—core position, orientation of the surrounding streamlines, and late-phase reconfiguration—is equivalently captured by both techniques and at both cardiac outputs.

Together, the nondimensional speed maps of $|\mathbf{u}|^*$ and λ_2^* depict a consistent intraventricular sequence: (i) an early inflow jet below the mitral plane feeding a spiral motion in the apical region; (ii) a mid-diastolic phase characterized by reduced velocity but persistent vortex coherence; and (iii) a late-diastolic a near-valve re-acceleration accompanied by a vortex core reconfiguration. At higher flow regime (CO_5), these flow features appear with greater amplitude and spatial extent but preserving the same temporal ordering. Across both flow regimes, EBIV and PIV yield concordant patterns in jet path, vortex core location, and late-phase re-energization, demonstrating strong inter-technique consistency in the spatial kinematics and coherent structure identification.

B. Velocity magnitude and pulsatile kinetic energy trends

The phase evolution of the nondimensional velocity magnitude ($|\mathbf{u}|^*$) and phase-locked kinetic energy (PKE^*) averaged over three distinct LV regions of interest (ROIs)—submitral, apex, and nearby the outflow—are shown in Fig. 11, where the phase origin corresponds to the E-wave peak ($\phi = 0$).

At flow regime $CO_{3.5}$, the LV outflow exhibits an early maximum in $|\mathbf{u}|^*$ in the range of $\pi/3 \leq \phi \leq 2\pi/3$, followed by a gradual decay [Fig. 11(a)]. This behavior reflects the forward drift and subsequent deceleration of the transmitral jet after the onset of the diastolic filling

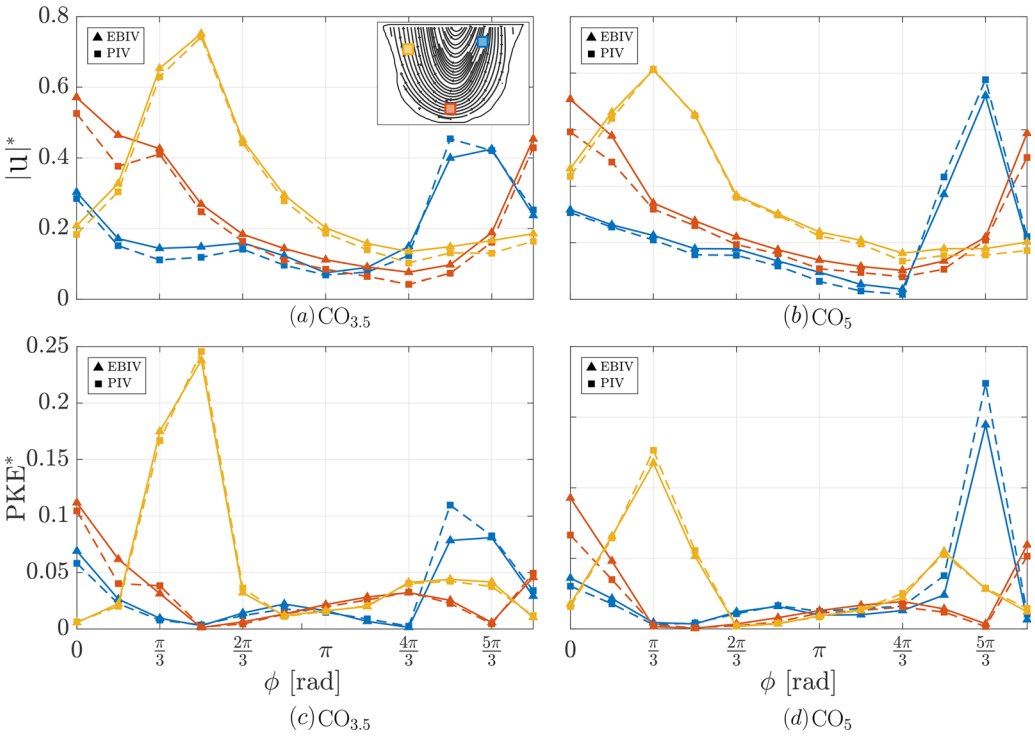

FIG. 11. Trends across three ROIs: submitral (blue), apical (red), and near-outflow (yellow). (a) and (b) Phase evolution of the normalized velocity magnitude $|\mathbf{u}|^*$ averaged over the ROIs. (c) and (d) Phase evolution of the normalized phase-locked kinetic energy PKE^* over the same ROIs. Curves are shown for EBIV (triangles) and PIV (squares). The phase origin is set at the E-wave peak ($\phi = 0$).

($\phi = 0$). In the LV submitral region, $|\mathbf{u}|^*$ starts relatively high at $\phi = 0$, decreases to a mid-diastolic minimum, and then raises again around $\phi \approx 5\pi/3$ (Fig. 11), consistently with the late inflow that occurs as the mitral valve reopens, around $\phi = 3\pi/2$. In contrast, the LV apex region shows gradual increase toward its peak with smoother, broader maxima, indicating a slower momentum build-up in the apical region rather than a consistently lower amplitude. The corresponding PKE* trends preserve the same ordering and phase dependence—an early maximum in the outflow region, low mid-diastolic levels, and a small late enhancement primarily below the mitral plane [Fig. 11(c)]. Across all the three LV regions, EBIV and PIV data remain closely aligned in both phase and amplitude.

At higher flow regime (CO_5), the qualitative sequence remains the same, but amplitudes increase and phase transitions sharpen. The LV outflow region again shows a clear early peak around $\phi \approx \pi/3$, while the submitral region presents a pronounced late rise around $\phi \approx 5\pi/3$ [Fig. 11(b)]. The apex region retains smoother, with more gradual variations. The PKE* distributions mirror these dynamics, concentrating coherent kinetic energy early in the outflow side region and exhibiting a late re-energization below the mitral valve [Fig. 11(d)]. Taken together, the regional trends outline a consistent intraventricular sequence: (i) energy injection near the mitral plane during the E-wave; (ii) partial transport toward the outflow side during early diastole; and (iii) a late contribution below the mitral valve as filling resumes, while the LV apex remains comparatively weakly energized.

Across both flow regimes, EBIV and PIV demonstrate excellent agreement in phase alignment, amplitude, and curve morphology, with no discernible phase shift. Minor discrepancies are observed only locally and primarily in correspondence with rapid changes in velocity, such as during the onset of the E-wave in the submitral region. Increasing cardiac output amplifies magnitudes but preserves the temporal sequence, confirming the robustness and mutual consistency of the phase-locked description of velocity and coherent energy obtained from both modalities.

C. Flow circulation

The phase evolution of the circulation per unit area, $\langle\Gamma\rangle^{(\phi)}$, obtained from both measurement techniques and for both flow regimes, is presented in Fig. 12. Also, in this case, the phase origin is set at the E-wave peak ($\phi = 0$). Negative values throughout diastole indicate a clockwise rotation of the main diastolic vortex in the aortomitral plane.

Across all conditions, the trends display consistent qualitative patterns. Immediately at $\phi = 0$, the magnitude of $\langle\Gamma\rangle^{(\phi)}$ reaches its minimum, reflecting the rapid shear roll-up at the mitral orifice and the formation of the diastolic vortex ring. Thereafter, $\langle\Gamma\rangle^{(\phi)}$ increases steadily toward less-negative values through early and mid-diastole, approaching a broad near-plateau around $\phi \simeq \pi$–$4\pi/3$. A mild downturn appears toward late diastole ($\phi \gtrsim 5\pi/3$), consistent with vortex weakening and pre-systolic reorganization.

The comparison between techniques reveals nearly identical temporal behavior. EBIV and PIV follow nearly identical trajectories, with coincident phase timing and comparable amplitudes throughout the cardiac cycle. Flow circulation data from the two measurement techniques overlap closely in the mid-diastolic plateau, confirming that the event-based reconstruction reproduces the same phase-averaged dynamics captured by PIV. EBIV variations appear slightly smoother, particularly during the deceleration phase, but without any appreciable loss of amplitude or phase coherence. Quantitatively, the main statistics are summarized in Table II. For both flow regimes, the minima of $\langle\Gamma\rangle^{(\phi)}$ occur at $\phi = 0$, and EBIV-PIV differences remain within $\sim$5%–7% for both the minima and the cycle-averaged circulation.

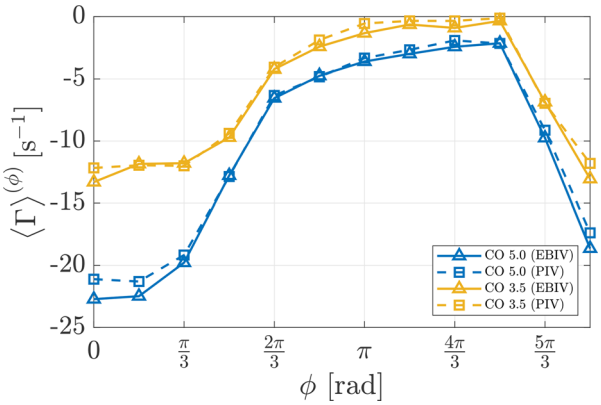

FIG. 12. Phase evolution of the circulation per unit area, $\langle\Gamma\rangle^{(\phi)}$, for EBIV and PIV at CO_5 and $CO_{3.5}$. The phase origin ($\phi = 0$) corresponds to the E-wave peak; negative values indicate a clockwise vortex rotation on the aortomitral plane.

The influence of flow regime is evident from the amplitude and slope. At CO_5, the initial minimum is deeper and the subsequent rise steeper, indicating stronger vorticity generation driven by the higher inflow momentum. At $CO_{3.5}$, the range is smaller and the transition to the plateau more gradual, consistent with weaker but more persistent recirculation. Both EBIV and PIV reproduce this dependence on cardiac output with identical phase timing and comparable magnitudes, underscoring robustness and reliability of the circulation quantity.

D. Lagrangian analysis

To evaluate the agreement between velocity fields obtained via EBIV and PIV measurement, a Lagrangian analysis was also performed. Virtual tracer particles were seeded at specified initial positions (x_0, y_0) and advected through the domain using both the two differently measured velocity datasets. At each integration step, the instantaneous velocity components (u, v) were interpolated spatially on the native rectilinear grid of each technique, avoiding any resampling between fields to prevent additional smoothing artifacts introduced by mapping. Particle motion was terminated once trajectories exited the common overlap region of the two measured domains.

To enhance trajectory smoothness, temporal interpolation was applied between successive velocity fields. Given that twelve phase-locked snapshots were available per cardiac cycle, the sampling rate

TABLE II. Circulation per unit area, $\langle\Gamma\rangle^{(\phi)}$ s^{-1}: minimum at $\phi = 0$ and cycle-averaged value.

	CO_5			$CO_{3.5}$		
Metric	EBIV	PIV	% diff	EBIV	PIV	% diff
$\min\langle\Gamma\rangle^{(\phi)}$	−22.7	−21.3	6.6	−13.3	−12.7	4.7
$\overline{\langle\Gamma\rangle}$	−10.7	−10.2	4.9	−6.3	−5.9	6.8

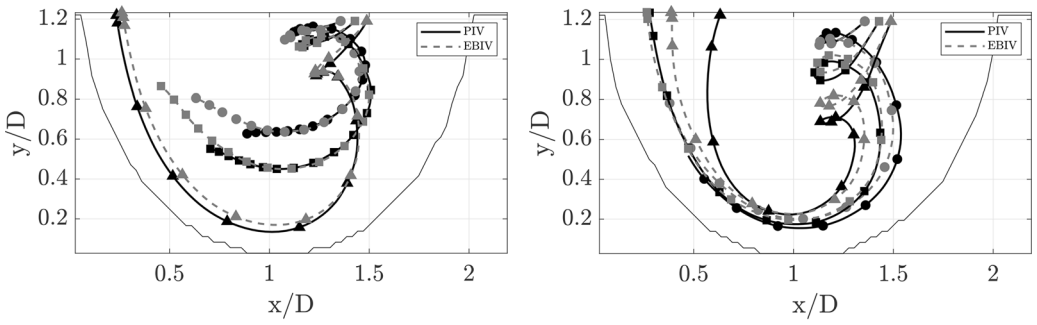

(a) $CO_{3.5}$ (b) CO_5

FIG. 13. Lagrangian trajectories at $CO_{3.5}$ and CO_5—panels (a) and (b), respectively—normalized by the diameter of the mitral valve, *D*. Solid black lines denote PIV trajectories, while dashed gray lines denote EBIV; distinct markers indicate different initial seeds.

satisfied the Nyquist criterion for the dominant flow frequencies, allowing smooth temporal reconstruction of particle motion. Trajectories were integrated using a second-order midpoint (Runge–Kutta 2) scheme with a sub–time step $\Delta t_{sub} = \Delta t/10$, ensuring temporal accuracy throughout the integration process.

The resulting trajectories for flow regimes $CO_{3.5}$ and CO_5 are shown in Fig. 13. At $CO_{3.5}$, the agreement between PIV and EBIV trajectories is evident: EBIV accurately reproduces the flow topology, including recirculation zone and trajectory curvature, with only minor deviations. EBIV trajectories appear smoother and slightly more centered along the upward branch—an effect attributed to the inherent noise-filtering properties of event-based reconstruction. This smoother behavior originates from the asynchronous acquisition mechanism of event-based sensors, which register events only when local brightness changes exceed a contrast threshold. Static regions thus generate no events, and only dynamically illuminated tracer particles contribute to the pseudo-images used for cross-correlation. This feature reduces background noise, improves the signal-to-noise ratio, and mitigates decorrelation effects commonly observed in conventional frame-based imaging. Such properties have been previously demonstrated in EBIV studies, showing that event-based velocimetry reproduces coherent fluid structures with reduced data redundancy and increased robustness to illumination fluctuations.[30–32]

When comparing the two operating flow regimes, the CO_5 condition exhibits greater trajectory curvature and spatial extent, consistent with the higher kinetic energy and inflow momentum of the more energetic regime. Nonetheless, the agreement between PIV and EBIV remains strong in both cases, confirming that EBIV can reliably reproduce Lagrangian flow features across distinct dynamic conditions. EBIV and PIV trajectories showed minor discrepancies at the higher cardiac output (CO_5). This is attributable to (i) higher velocity and shear levels, which increase the sensitivity of correlation-based estimates to small local differences between datasets and (ii) the cumulative nature of Lagrangian integration, whereby the contribution of minor instantaneous discrepancies can pileup over time. Nevertheless, EBIV and PIV trajectories remain markedly consistent in terms of global transport pathways and recirculation topology.

E. Proper orthogonal decomposition-based analysis

The cumulative explained variance (CEV) of POD modes evolves almost identically for EBIV and PIV measurements, at the two distinct flow regimes $CO_{3.5}$ and CO_5 (Fig. 14). Because CEV values are normalized to the PIV total energy, the EBIV curve saturates at

$$\eta = \frac{\sum_{k=1}^{N} \sigma^2_{k,\mathrm{EBIV}}}{\sum_{k=1}^{N} \sigma^2_{k,\mathrm{PIV}}}, \tag{21}$$

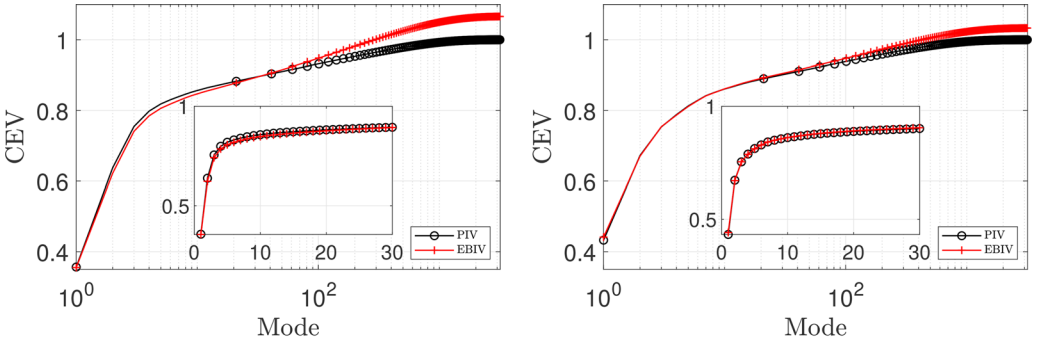

(a) $CO_{3.5}$ (b) CO_5

FIG. 14. Comparison of cumulative explained variance (CEV) profiles at different cardiac outputs (a) $CO_{3.5}$ and (b) CO_5 for PIV and EBIV data.

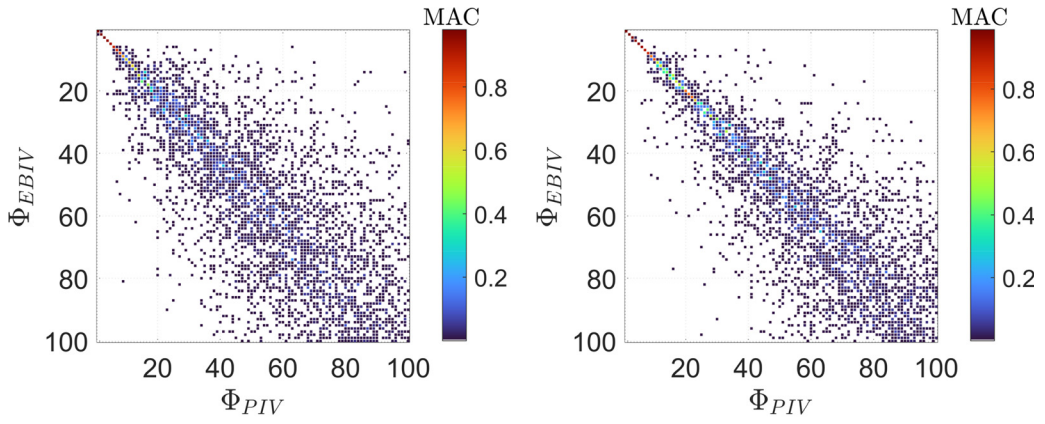

FIG. 15. Modal assurance criterion (MAC) matrices for the PIV and EBIV first 100 POD modes at $CO_{3.5}$ (a) and CO_5 (b).

where σ_k denotes the eigenvalue associated with the k-th POD mode. For the $CO_{3.5}$ flow regime, $\eta > 1$, indicating that EBIV is characterized by a slightly larger total velocity variance, primarily distributed in higher-order modes. This behavior stems from local edge enhancement and event saturation effects in the pseudo-frames—features commonly reported in event-based imaging studies.[28] For the leading modes, the EBIV and PIV CEV curves remain closely aligned, with both capturing over 80% of the total velocity variance within the first 10–15 modes. This confirms that both techniques recover the same dominant fluid structures and preserve their energetic hierarchy. Beyond approximately 10 modes, the EBIV curve increases more steeply than PIV, reflecting a redistribution of energy toward higher-dimensional components due to event-level noise. The overshoot is less pronounced at flow regime CO_5 ($\eta \approx 1$), which can be attributed to the higher signal-to-noise ratio of the EBIV data under this operating flow condition and to an energy concentration in the leading modes, driven by the stronger LV inflow dynamics.

The MAC matrices for the two flow regimes $CO_{3.5}$ and CO_5 (Fig. 15) further support this interpretation: both display a strong diagonal dominance for the leading modes ($MAC_{ij} \geq 0.9$), demonstrating that EBIV and PIV recover essentially identical dominant spatial structures. At flow regime $CO_{3.5}$, the MAC matrix exhibits a pronounced diagonal with mild off-diagonal leakage close to nearly degenerate mode pairs (mode swapping), consistent with similar energetic content and small SNR penalties. Localized off-diagonal patches indicate minor order ambiguity, but these do not affect the low-dimensional subspace—the subspace MAC for $r \leq 10$ remains high. At flow regime CO_5, diagonal dominance strengthens and off-diagonal terms weaken, yielding slightly higher MAC values for the leading modes. This finding reflects the enhanced EBIV SNR and greater cycle-to-cycle coherence at higher flow rates, both of which reduce modal mixing. Overall, the off-diagonal entries remain low across conditions, implying a consistent modal hierarchy and limited mode mixing between techniques. High diagonal MAC values validate the equivalence of the spatial bases extracted from EBIV and PIV measurements.

Taken together, the MAC and CEV analyses demonstrate that EBIV and PIV share nearly identical low-order modal subspaces. The leading modes from both techniques represent the same coherent flow structures and contribute comparably to the total velocity variance of the flow field. These results indicate that EBIV preserves not only the spatial organization of the dominant structures, but also their energetic hierarchy, thereby faithfully reproducing the essential modal content of the flow. This confirms the consistency of EBIV with PIV and underscores its suitability for reduced-order analysis of intraventricular fluid dynamics.

IV. CONCLUSIONS

This study provides a comprehensive experimental validation of EBIV in the complex scenario of cardiac fluid dynamics. Using a physiologically representative LV heart simulator loop equipped with a transcatheter mitral valve prosthesis, EBIV measurements were directly compared against the reference standard, the frame-based PIV measurements at two different flow regimes under identical acquisition and processing conditions, ensuring strict methodological consistency. Across a large arsenal of fluid mechanics quantities—phase-averaged velocity fields, vorticity distributions, circulation, reconstructed Lagrangian trajectories, phase-locked kinetic energy, and modal content—EBIV demonstrated close agreement with PIV. The event-based approach faithfully reproduced the topology and temporal evolution of the LV diastolic vortex, including formation below the mitral plane, translation toward the apex and late-diastolic reorientation toward the LV outflow tract—while preserving the phase evolution of circulation and Lagrangian trajectories. Deviations between the two techniques were minor and did not affect the physical interpretation of LV fluid dynamics.

Modal analysis further reinforced these findings. POD returned nearly identical spatial modal bases for EBIV and PIV—a moderate overshoot in the EBIV velocity variance tail, attributed to noise or edge-enhancement effects in pseudo-frames, was reduced at $5.0\,\mathrm{l\,min^{-1}}$, consistent with the improved SNR conditions. Crucially, the low-order modal subspace, which contains the dominant coherent structures, remained shared across techniques.

A central advantage of EBIV lies in its data efficiency and temporal precision. By asynchronously recording pixel-level brightness changes, EBIV suppresses redundant information and produces orders-of-magnitude smaller data volumes while retaining spatial resolution and

dynamic range. The pulsed-illumination strategy adopted here enabled strict synchronization and temporal coherence in velocity fields without compromising accuracy. Practically, EBIV offers additional advantages that are particularly relevant for *in vitro* cardiovascular testing. For example, the *in vitro* evaluation of the performance of prosthetic heart valves in mock circulatory loops often requires repeated measurements under multiple operating conditions, long acquisition times, and strict phase locking. Compared to conventional PIV systems, EBIV enables quantitative flow measurements with more compact and generally less expensive imaging hardware than conventional PIV systems, while substantially reducing data throughput. Although these aspects does not directly affect measurement accuracy, it has remarkable implications for the intended context of use of EBIV in cardiovascular devices testing, including rapid screening of valve designs, iterative optimization, and extended experimental campaigns that would be operationally more demanding with frame-based PIV systems.

However, EBIV presents specific challenges for fluid-mechanical measurements. The asynchronous sensing mechanism may introduce latency and timing jitter at very high frequencies. Moreover, low-contrast or sparsely seeded regions may produce insufficient events, and extremely dynamic scenarios can lead to event saturation if the sensor bandwidth is exceeded. As a relatively new technique, EBIV still requires continued refinement, particularly in bias tuning, noise-control strategies, and standardized acquisition protocols.

Notwithstanding these limitations, the findings of this study demonstrate that EBIV can be a reliable, compact, and data-efficient alternative to PIV for quantitative investigations of pulsatile cardiac flows and for the assessment of heart valve prostheses. The strong agreement with PIV across Eulerian quantities, energetic trends, Lagrangian trajectories, and modal content suggests that EBIV is well suited for applications involving real-time flow control, device optimization, and reduced-order or physics-informed modeling in cardiovascular research.

ACKNOWLEDGMENTS

The research leading to these results received funding from the European Union—NextGenerationEU through the Italian Ministry of University and Research under PNRR the M4C2-I1.3 Project PE_00000019 "HEAL ITALIA" to Umberto Morbiducci and Manuel Zannone (No. CUP E93C22001860006).

AUTHOR DECLARATIONS

Conflict of Interest

The authors have no conflicts to disclose.

Author Contributions

E. Amico: Conceptualization (equal); Data curation (equal); Formal analysis (equal); Investigation (equal); Methodology (equal); Validation (equal); Visualization (equal); Writing – original draft (equal); Writing – review & editing (equal). **M. Zannone:** Conceptualization (equal); Data curation (equal); Formal analysis (equal); Investigation (equal); Methodology (equal); Validation (equal); Visualization (equal); Writing – original draft (equal); Writing – review & editing (equal). **E. Torta:** Investigation (equal); Writing – review & editing (equal). **G. Mastronuzzi:** Formal analysis (equal); Writing – review & editing (equal). **D. Pecchio:** Resources (supporting). **D. Gallo:** Conceptualization (equal); Resources (equal); Writing – review & editing (equal). **J. Serpieri:** Writing – review & editing (equal). **G. Cafiero:** Conceptualization (equal); Resources (equal); Writing – review & editing (equal). **U. Morbiducci:** Conceptualization (equal); Resources (equal); Writing – original draft (equal); Writing – review & editing (equal).

DATA AVAILABILITY

The data that support the findings of this study are available from the corresponding author upon reasonable request.

REFERENCES

[1]X. Wu, H. Saaid, J. Voorneveld, T. Claessens, J. J. Westenberg, N. de Jong, J. G. Bosch, and S. Kenjereš, "4D flow patterns and relative pressure distribution in a left ventricle model by shake-the-box and proper orthogonal decomposition analysis," Cardiovasc. Eng. Technol. **14**, 743–754 (2023).
[2]V. Vu and K. May-Newman, "Fluid mechanics of aortic valve incompetence in the dilated left ventricle," Front. Med. Eng. **2**, 1326800 (2024).
[3]L. Liu, C. Wu, W. Liu, W. Zou, Y. Zheng, C. Wang, and Y. Zhang, "Dynamics of transcatheter heart valves with an *in vitro* experiment incorporating particle image velocimetry," AIP Adv. **11**, 105301 (2021).
[4]J.-P. Rabbah, N. Saikrishnan, and A. P. Yoganathan, "A novel left heart simulator for the multi-modality characterization of native mitral valve geometry and fluid mechanics," Ann. Biomed. Eng. **41**, 305–315 (2013).
[5]A. Darwish, C. Papolla, R. Rieu, and L. Kadem, "An anatomically shaped mitral valve for hemodynamic testing," Cardiovasc. Eng. Tech. **15**, 374–381 (2024).
[6]G. Pedrizzetti and F. Domenichini, "Left ventricular fluid mechanics: The long way from theoretical models to clinical applications," Ann. Biomed. Eng. **43**, 26–40 (2015).
[7]B. Baccani, F. Domenichini, and G. Pedrizzetti, "Vortex dynamics in a model left ventricle during filling," Eur. J. Mech. B/Fluids **21**, 527–543 (2002).
[8]B. Baccani, F. Domenichini, and G. Pedrizzetti, "Model and influence of mitral valve opening during the left ventricular filling," J. Biomech. **36**, 355–361 (2003).
[9]A. P. Yoganathan, Z. He, and S. Casey Jones, "Fluid mechanics of heart valves," Annu. Rev. Biomed. Eng. **6**, 331–362 (2004).
[10]M. S. Nagargoje, E. Lazpita, J. Garicano-Mena, and S. Le Clainche, "A review on vortex dynamics in the healthy and dilated left ventricles and its application to heart health," Flow **5**, E10 (2025).
[11]D. Mele, L. Serio, R. Beccari *et al.*, "Left ventricular flow dynamics by cardiac imaging techniques in heart failure patients: State of the art," Cardiovasc. Ultrasound **23**, 13 (2025).
[12]A. Kheradvar, G. Pedrizzetti *et al.*, "Vortex formation in the left ventricle: Quantitative methods and clinical relevance," J. Cardiol. **74**, 403–243 (2019).
[13]G.-R. Hong, G. Pedrizzetti, G. Tonti, P. Li, Z. Wei, J. K. Kim, A. Baweja, S. Liu, N. Chung, H. Houle, J. Narula, and M. A. Vannan, "Characterization and quantification of vortex flow in the human left ventricle by contrast echocardiography using vector particle image velocimetry," JACC Cardiovasc. Imaging **1**, 705–717 (2008).
[14]F. Domenichini, G. Pedrizzetti, and B. Baccani, "Combined experimental and numerical analysis of the flow structure into the left ventricle," J. Biomech. **40**, 1988–1994 (2007).
[15]C. Özcan, Ö. Kocatürk, C. Işlak, and C. Öztürk, "Integrated particle image velocimetry and fluid–structure interaction analysis for patient-specific abdominal aortic aneurysm studies," Biomed. Eng. Online **22**, 113 (2023).
[16]Y. Li, D. I. Verrelli, W. Yang, Y. Qian, and W. Chong, "A pilot validation of CFD model results against PIV observations of haemodynamics in intracranial aneurysms treated with flow-diverting stents," J. Biomech. **100**, 109590 (2020).
[17]G. Querzoli, S. Fortini, and A. Cenedese, "Effect of the prosthetic mitral valve on vortex dynamics and turbulence of the left ventricular flow," Phys. Fluids **22**, 041901 (2010).
[18]Y. Qiang, T. Duan, M. Zhang, L. Qi, L. Wei, and W. Zhong, "Impact of bileaflet mechanical heart valve leaflet dysfunction on left ventricular blood flow: An experimental study," Phys. Fluids **35**, 091909 (2023).

[19]Y. Qiang, Z. Li, M. Zhang, T. Duan, L. Qi, L. Wei, and W. Zhong, "Effect of leaflet shape on the left ventricular blood flow pattern in BMHVS," Exp. Therm. Fluid Sci. **161**, 111343 (2025).
[20]O. Pierrakos, P. P. Vlachos, and D. P. Telionis, "Time-resolved DPIV analysis of vortex dynamics in a left ventricular model through bileaflet mechanical and porcine heart valve prostheses," J. Biomech. Eng. **126**, 714–726 (2004).
[21]H. Saaid, P. Segers, M. Novara, T. Claessens, and P. Verdonck, "Single calibration multiplane stereo-PIV: The effect of mitral valve orientation on three-dimensional flow in a left ventricle model," Exp. Fluids **59**, 49 (2018).
[22]G. Maraouch and L. Kadem, "Flow dynamics in a model of a left ventricle with different mitral valve orientations," Fluids **6**, 428 (2021).
[23]C. Papolla, A. Darwish, L. Kadem, and R. Rieu, "Impact of mitral regurgitation on the flow in a model of a left ventricle," Cardiovasc. Eng. Technol. **11**, 708–718 (2020).
[24]G. Di Labbio and L. Kadem, "Jet collisions and vortex reversal in the human left ventricle," J. Biomech. **78**, 155–160 (2018).
[25]H. Saaid, J. Voorneveld, C. Schinkel, J. Westenberg, F. Gijsen, P. Segers, P. Verdonck, N. de Jong, J. G. Bosch, S. Kenjeres *et al.*, "Tomographic PIV in a model of the left ventricle: 3D flow past biological and mechanical heart valves," J. Biomech. **90**, 40–49 (2019).
[26]C. Posch, T. Serrano-Gotarredona, B. Linares-Barranco, and T. Delbruck, "Retinomorphic event-based vision sensors: Bioinspired cameras with spiking output," Proc. IEEE **102**, 1470–1484 (2014).
[27]P. Lichtsteiner, C. Posch, and T. Delbruck, "A 128 × 128 120 db 15 μs latency asynchronous temporal contrast vision sensor," IEEE J. Solid-State Circuits **43**, 566–576 (2008).
[28]L. Franceschelli, C. E. Willert, M. Raiola, and S. Discetti, "An assessment of event-based imaging velocimetry for efficient estimation of low-dimensional coordinates in turbulent flows," Exp. Therm. Fluid Sci. **164**, 111425 (2025).
[29]G. Gallego, T. Delbrück, G. Orchard, C. Bartolozzi, B. Taba, A. Censi, S. Leutenegger, A. J. Davison, J. Conradt, K. Daniilidis, and D. Scaramuzza, "Event-based vision: A survey," IEEE Trans. Pattern Anal. Mach. Intell. **44**, 154–180 (2022).
[30]C. E. Willert and J. Klinner, "Event-based imaging velocimetry: An assessment of event-based cameras for the measurement of fluid flows," Exp. Fluids **63**, 103 (2022).
[31]C. E. Willert, "Event-based imaging velocimetry using pulsed illumination," Exp. Fluids **64**, 98 (2023).
[32]L. Franceschelli, E. Amico, M. Raiola, C. Willert, J. Serpieri, G. Cafiero, and S. Discetti, "Event-based imaging velocimetry for jet flow control," in 16th International Symposium on Particle Image Velocimetry (ISPIV), 2025.
[33]International Organization for Standardization, "Cardiovascular implants—Cardiac valve prostheses—Part 1: General requirements," Standard No. ISO 5840-1:2021 (ISO, Geneva, Switzerland, 2021).
[34]A. Medical, see https://www.affluentmedical.com/epygon-3/ for "Epygon—Physiological Transcatheter Mitral Prosthesis" (accessed September 10, 2025).
[35]M. Scorsin, M. Andreas, S. Corona, A. C. Guta, P. Aruta, and L. P. Badano, "Novel transcatheter mitral prosthesis designed to preserve physiological ventricular flow dynamics," Ann. Thoracic Surg. **113**, 593–599 (2022).
[36]ClinicalTrials.gov, see https://clinicaltrials.gov/study/NCT04775108 for "Minimally Invasive EPYGON Mitral Valve First-in-Human Evaluation (MINERVA), Identifier: NCT04775108" (accessed September, 2025).
[37]A. V. Oppenheim and R. W. Schafer, *Discrete-Time Signal Processing*, 3rd ed. (Pearson, 2009).
[38]L. Maya, L. Fan, A. Durocher, B. Savard, and P. Vena, "An evaluation of event-based cameras for particle image velocimetry," Exp. Fluids **66**, 204 (2025).
[39]R. J. Adrian and J. Westerweel, *Particle Image Velocimetry* (Cambridge University Press, 2011).
[40]T. Astarita and G. Cardone, "Analysis of interpolation schemes for image deformation methods in PIV," Exp. Fluids **38**, 233–243 (2005).
[41]T. Astarita, "Analysis of interpolation schemes for image deformation methods in PIV: Effect of noise on the accuracy and spatial resolution," Exp. Fluids **40**, 977–987 (2006).
[42]T. Astarita, "Analysis of weighting windows for image deformation methods in PIV," Exp. Fluids **43**, 859–872 (2007).
[43]T. Astarita, "Analysis of velocity interpolation schemes for image deformation methods in PIV," Exp. Fluids **45**, 257–266 (2008).
[44]T. Astarita, "Adaptive space resolution for PIV," Exp. Fluids **46**, 1115–1123 (2009).
[45]R. Giordano and T. Astarita, "Spatial resolution of the stereo PIV technique," Exp. Fluids **46**, 643–658 (2009).
[46]G. Paolillo and T. Astarita, "Perspective camera model with refraction correction for optical velocimetry measurements in complex geometries," IEEE Trans. Pattern Anal. Mach. Intell. **44**, 3185–3196 (2022).
[47]G. Paolillo and T. Astarita, "On the PIV/PTV uncertainty related to calibration of camera systems with refractive surfaces," Meas. Sci. Technol. **32**, 094006 (2021).
[48]J. Jeong and F. Hussain, "On the identification of a vortex," J. Fluid Mech. **285**, 69–94 (1995).
[49]P. Baj, P. J. K. Bruce, and O. R. H. Buxton, "The triple decomposition of a fluctuating velocity field in a multiscale flow," Phys. Fluids **27**, 075104 (2015).
[50]C. S. Greco, G. Cardone, and J. Soria, "On the behaviour of impinging zero-net-mass-flux jets," J. Fluid Mech. **810**, 25–59 (2017).
[51]L. Sirovich, "Turbulence and the dynamics of coherent structures. I—Coherent structures. II—Symmetries and transformations. III—Dynamics and scaling," Q. Appl. Math. **45**, 561–571 (1987).
[52]G. Berkooz, P. Holmes, and J. L. Lumley, "The proper orthogonal decomposition in the analysis of turbulent flows," Annu. Rev. Fluid Mech. **25**, 539–575 (1993).
[53]K. Taira, S. L. Brunton, S. T. M. Dawson, C. W. Rowley, T. Colonius, B. J. McKeon, O. T. Schmidt, S. Gordeyev, V. Theofilis, and L. S. Ukeiley, "Modal analysis of fluid flows: An overview," AIAA J. **55**, 4013–4041 (2017).
[54]J. N. Kutz, *Data-Driven Modeling and Scientific Computation: Methods for Complex Systems and Big Data* (Oxford University Press, Oxford, UK, 2016).
[55]E. Lazpita *et al.*, "Characterizing intraventricular flow patterns via modal decomposition techniques," arXiv:2507.21651 (2025).